

Supplementary information for:

**Imaging Bacterial Inter-Species Chemical Interactions
by Surface Enhanced Raman Scattering**

Gustavo Bodelón,^a Verónica Montes-García,^a Celina Costas,^a Ignacio Pérez-Juste,^a
Jorge Pérez-Juste,^a Isabel Pastoriza-Santos^a and Luis M. Liz-Marzán^{a,b,c,d}

^a Departamento de Química Física and CINBIO, Universidade de Vigo, 36310 Vigo,
Spain

^b Bionanoplasmonics Laboratory, CIC biomaGUNE, Paseo de Miramón 182, 20014
Donostia-San Sebastián, Spain

^c Ikerbasque, Basque Foundation for Science, 48013 Bilbao, Spain

^d Biomedical Research Networking Center in Bioengineering, Biomaterials, and
Nanomedicine (CIBER-BBN), 20014 Donostia-San Sebastián, Spain

Section S1. Characterization of the plasmonic substrates. Pages S2-S3.

**Section S2. Theoretical study of Violacein: Conformational analysis, UV-Visible-
NIR and Raman Spectroscopic characterization. Pages S4-S14.**

**Section S3. SERS/SERRS detection of metabolites, bacterial culture on Au@agar
and qPCR procedure. Pages S15-S25.**

References. Pages S26-S27.

Section S1. Characterization of the plasmonic substrates

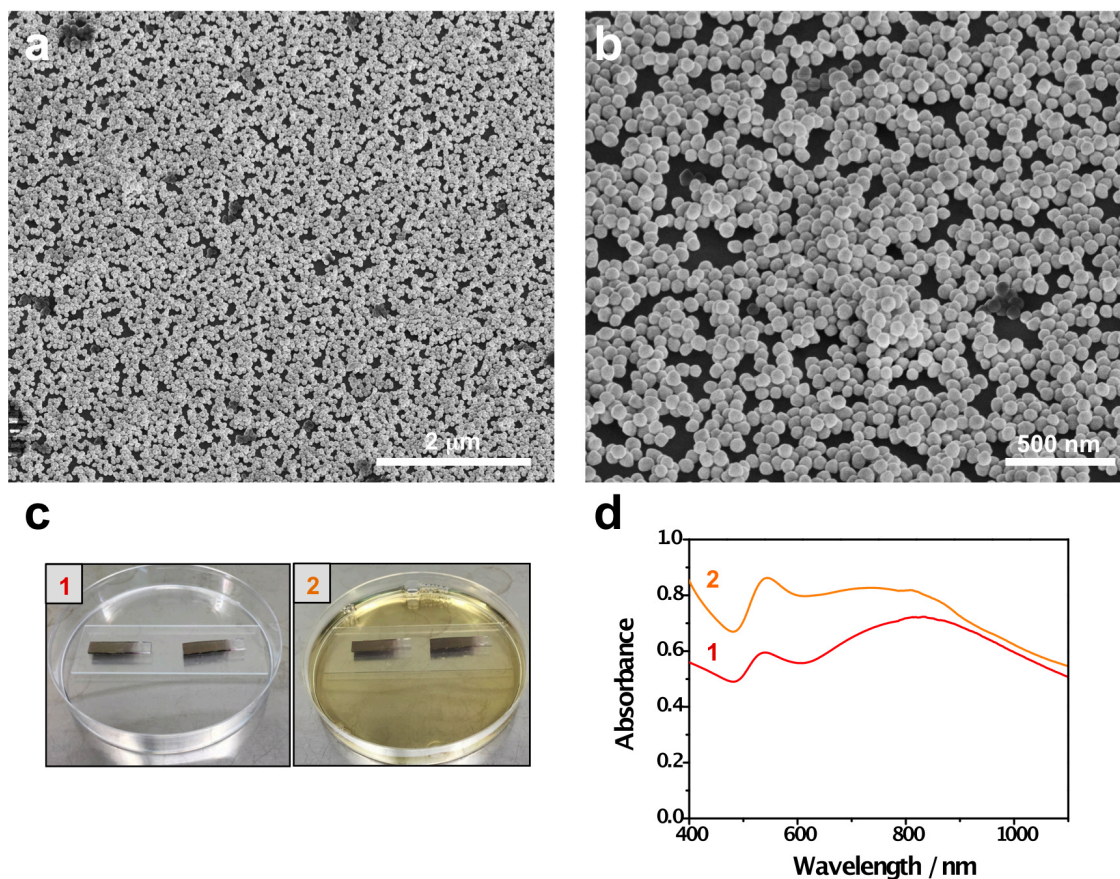


Figure S1. Substrate fabrication and optical properties of Au@agar substrate. (a and b). Scanning electron microscopy images of the submonolayer of gold nanospheres (60 nm) deposited on glass. **(c)** Photographs of the plasmonic layer on a glass slide inside a Petri dish, before (1) and after (2) the addition of LB agar. **(d)** Optical properties of the plasmonic film before (1) and after (2) the addition of LB agar.

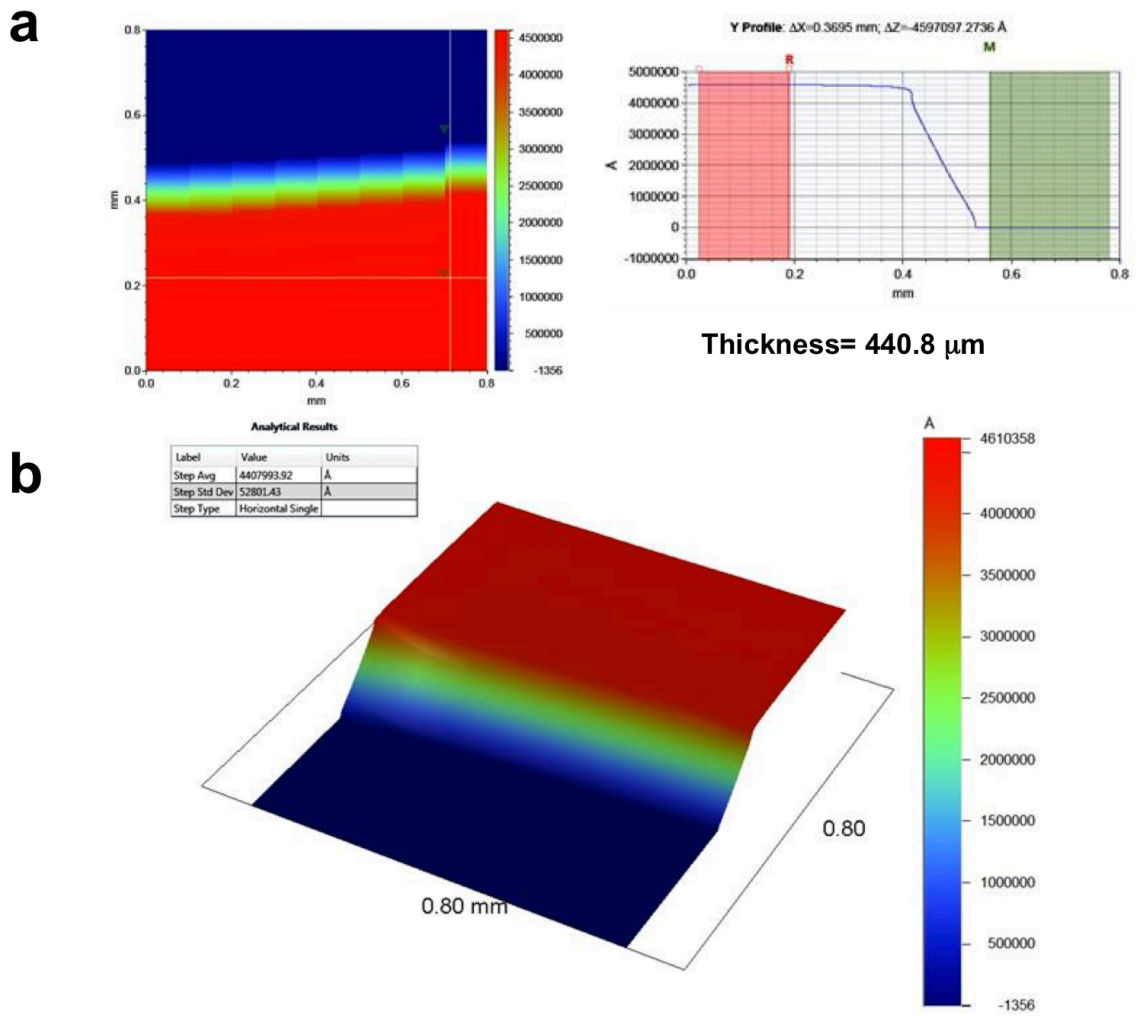
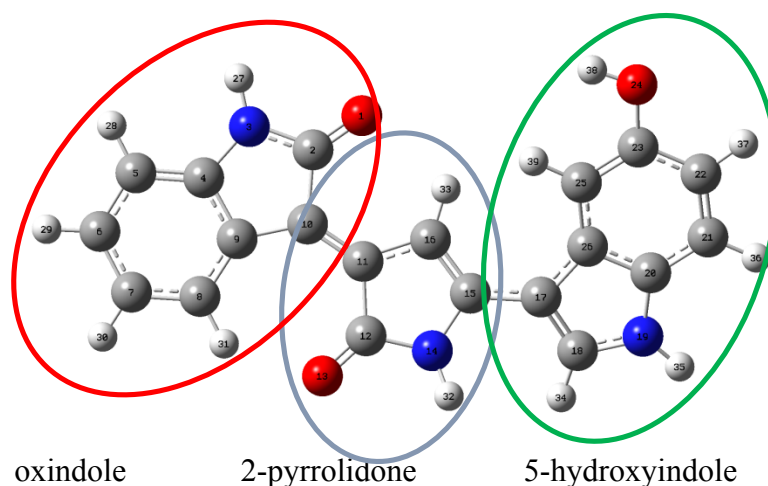


Figure S2. (a and b). Profilometry analysis of Au@agar. The average thickness of the agar layer was 441 μm .

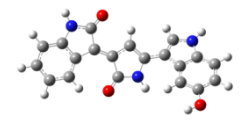
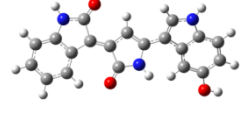
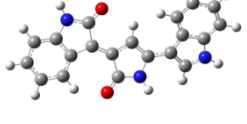
Section S2. Computational study of Violacein: Conformation analysis, UV-Visible-NIR and Raman Spectroscopic characterization

Conformation analysis of violacein. Violacein is composed by three heterocyclic units



The geometries of several structures with different relative orientations for the 5-hydroxyindole moiety and the hydroxyl group were optimized at the M062X/6-311++G** level, followed by characterization as energy minima by means of the analysis of vibrational frequencies. All the calculations were performed using Gaussian09.¹ Four stable conformations were determined (Supplementary Table 1), where the oxindole and 2-pyrrolidone units always keep planarity, whereas the 5-hydroxyindole group deviates from planarity by 20-30°, approximately.

Table S1. Results from the conformational analysis of violacein.

	Conformer	Total energy (a.u.)	Relative energy (kcal/mol)	Angle ^a
	TC	-1159.77511659	0.00	19.2
	CC	-1159.77398932	0.71	-28.9°
	CT	-1159.77314648	1.24	-27.2°
	TT	-1159.77280833	1.45	20.6

^a Angle formed between the coplanar oxindole-2-pyrrolidine units and the 5-hydroxyindole unit.

Absorption spectrum of violacein. The UV-vis spectrum in the gas phase for the most stable TC conformer was calculated by TDDFT, using the M062X and PBE0 functionals combined with the 6-311++G** basis set. The influence of the solvent (water) in the absorption spectrum was taken into account by using the Polarizable Continuum Model (PCM).¹ According to the best computational results, the spectrum is dominated by a broad band located at 532 nm, which would be in agreement with the experimental one, at 587 nm (see Supplementary Figure 3 and Table 2). Despite the deviation between the theoretical and experimental results, all the computational methods indicate that this band is originated by a π - π^* type electronic transition between the HOMO and LUMO represented in Figure 3 below. This electronic transition leads to redistribution of the electron density along the molecular framework, in particular within the resonant system formed by the coplanar oxindole and 2-pyrrolidone units.

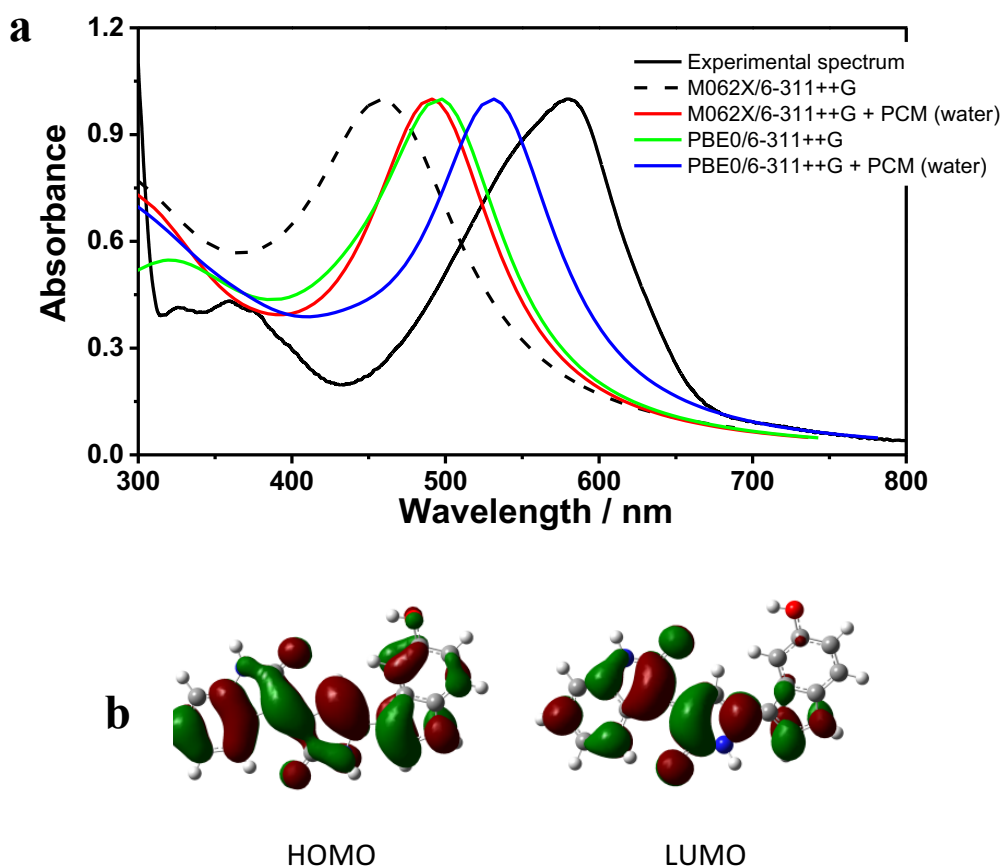


Figure S3. (a) Experimental and calculated absorption spectra of violacein. All spectra were normalized to unity at the maximum of the main band. (b) Representation of the HOMO-LUMO orbitals.

Table S2. Computational methods employed to obtain the UV-Vis-NIR spectrum of violacein, and maximum position of the main absorption band. The experimental value for this transition is also provided.

Theoretical method	λ_{\max} / nm
M062X/6-311++G**	460.4
M062X/6-311++G** + PCM (water)	491.3
PBE0/6-311++G**	497.7
PBE0/6-311++G** + PCM (water)	531.6
Experimental spectrum	587

Adsorption of violacein on a metallic surface. To study the adsorption of violacein on a metallic nanoparticle and to analyze its influence on the Raman spectrum we considered two different limiting geometrical models, with the violacein molecule oriented parallel and perpendicular to a metallic sheet formed by 22 gold atoms.

Geometrical optimizations at the M062X/6-311++G** level were performed for both limiting models, with violacein moving freely above the surface while keeping frozen the position of the gold atoms. Whereas the geometrical optimization for the parallel complex of violacein converged properly, the optimization of violacein adsorbed perpendicular on the metallic surface resulted in the parallel adsorption of violacein. The computed distance between violacein and the gold surface in the parallel complex is 3.3 Å. These calculations allowed us to determine an adsorption energy of ca. -42.9 kcal/mol (computed as $E_{\text{ads}} = E_{\text{complex}} - E_{\text{violacein}} - E_{\text{Au22}}$) for the parallel complex, much more favorable than the estimated vertical adsorption energy of $E_{\text{ads}} = -9.4$ kcal/mol.

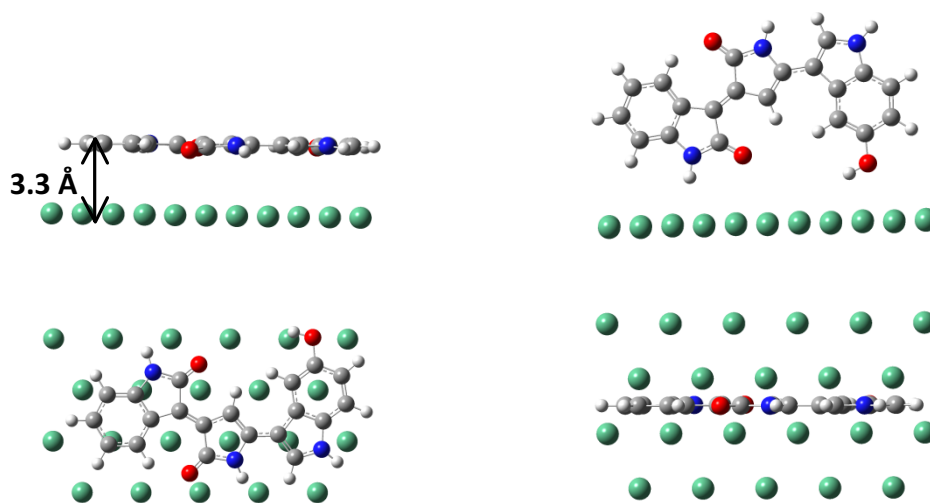


Figure S4. Geometries studied in the violacein adsorption on a Au metallic sheet, either parallel (left) or perpendicular (right).

Raman and SERS spectra of violacein. Vibrational analysis. The Raman spectrum for the most stable conformation of violacein TC was calculated employing the M062X/6-311++G** method. Supplementary Figure 5 shows excellent agreement between the theoretical and the experimental spectrum. A detailed assignment of the theoretical Raman spectrum to the molecular vibrational modes was performed by means of the VEDA program, which generates an optimized set of internal coordinates based on the molecular structure and provides a potential energy distribution for the quantitative analysis of vibrational spectra.² These results, shown in Supplementary Table 3 for those modes contributing more than 10% to the spectrum signals, allow us to provide a detailed assignment of the experimental Raman and SERS spectra and indicate that there is a significant coupling between vibrational modes as a consequence of the high conjugation along the molecular framework.

The experimental Raman spectrum is dominated by an intense band at 1132 cm⁻¹ that can be assigned to a mode involving the bending hydrogen atoms of the 5-hydroxindole ring (E) and the C-N stretching of the 2-pyrrolidone ring (C). The medium intensity band at 1548 cm⁻¹ would correspond to a C=C ring stretching of the (E) unit, while the doublet at 947 and 961 cm⁻¹ can be assigned to a mixed ring deformation of the oxindole unit (rings A, B) and a ring deformation of the (E) unit, and the band at 730 cm⁻¹ can be identified as a highly mixed ring CCC and CNC bending of the (C,A) moieties. Additional bands with smaller intensity can be also identified as hydrogen bending modes of the oxindole unit (rings A, B) at 1410 cm⁻¹, a C=C stretching of the (B) ring at 1221 cm⁻¹, a largely mixed deformation involving simultaneously the (C, D, E) rings at 1153 cm⁻¹, and a NCCC out-of-plane vibration of the central 2-pyrrolidone ring (C) at 680 cm⁻¹.

Upon adsorption, the relative intensity of some of the signals recorded in the SERS spectrum at 785 nm are specially enhanced (see Supplementary Figure 6). This is the case for the referred signals at 947, 1131, and 1549 cm⁻¹, as well as the band at 807 cm⁻¹, assigned to a deformation of the D,E rings, the signal at 873 cm⁻¹ which would also correspond to a deformation of the A,B rings, and the signal at 892 cm⁻¹ assigned to an in-plane deformation of the B,C rings. Significant relative enhancements can be also observed in the region of larger wavenumbers between 1200-1600 cm⁻¹, such as the signal at 1285 cm⁻¹, assigned to a bending motion of the hydrogen atoms of the E ring, the band at 1370 cm⁻¹ corresponding to the hydrogen bending of the (A) ring, the signal

at 1463 cm^{-1} associated to the ring (C,D) C-N stretchings and the band at 1608 cm^{-1} assigned to the stretching of the double C=C bond acting as a bridge between the B-C and C-D units.

It must be stressed that most of the signals with SERS enhancement upon adsorption correspond to in-plane vibrations parallel to the metallic surface. Interestingly, these vibrations appear mainly in the region between $600\text{-}800\text{ cm}^{-1}$, while for pyocyanin the in-plane ring deformations appear in the region between $400\text{-}600\text{ cm}^{-1}$, which allows the separate SERS detection of both compounds.

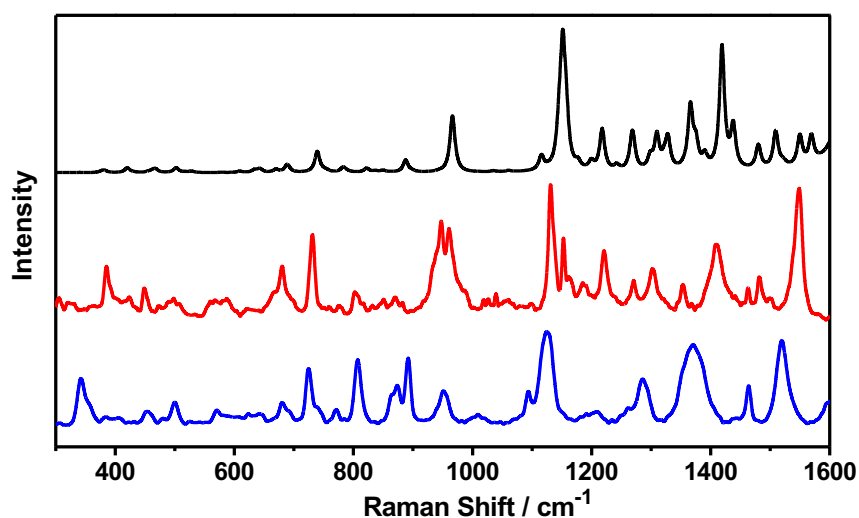


Figure S5. Calculated (black) and experimental (red) Raman spectra of violacein. Experimental SERS spectrum of violacein (blue) obtained at 785 nm excitation wavelength.

Finally, it is interesting to compare the predicted Raman spectra for complexes where violacein is adsorbed parallel and perpendicular to the metallic surface (Supplementary Figure 6). On one hand, for the perpendicular complex the Raman spectrum is dominated by a band around 1190 cm^{-1} , which, according Supplementary Table 2, would be associated to the H-OC bending mode of the hydroxyl group of the (E) ring and the H-NC bending mode of the (B) ring. This enhancement likely arises because these modes are associated to molecular regions closer to the surface in perpendicular orientation. However, and in agreement with experimental data, for the parallel orientation we see a general increase of the relative intensities of signals assigned to in-plane vibrations between $400\text{-}600\text{ cm}^{-1}$ and between $1200\text{-}1600\text{ cm}^{-1}$. This latter

observation reinforces the theoretical prediction about the energetic preference of the parallel adsorption of violacein on the metallic surface.

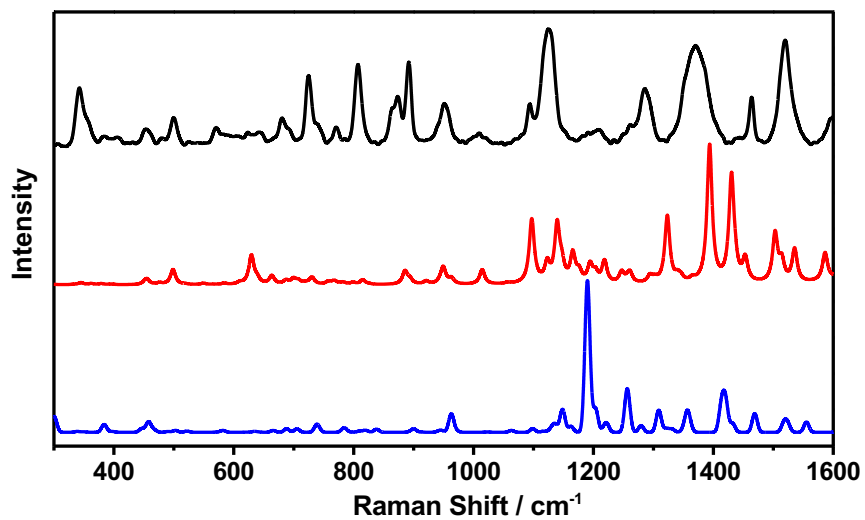
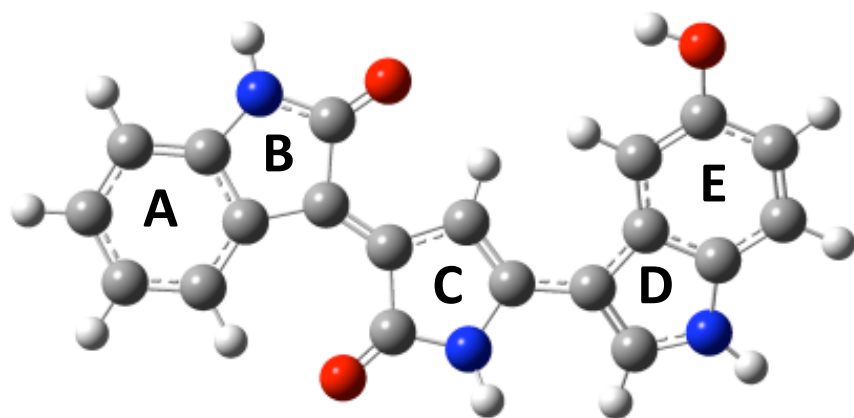


Figure S6. Experimental SERS spectrum (black) of violacein obtained at the 785 nm excitation wavelength, and calculated Raman spectra of violacein adsorbed parallel (red) and perpendicular (blue) to an Au sheet.



Supplementary Table 3. Experimental and calculated vibrational M062X/6-311++Gfrequencies**

Exp ^a	Exp(Si) _b	SERS ^c	Calculated ^d	Approximate description	Potential energy distribution
	305		310	HOCC out-of-plane torsion	90% ring (E) H-OCC torsion
		342	341	Ring twisting	50% ring (B) NCC and O=CN bending
			377	Ring deformation out-of-plane	20% rings (A,B) CCCC out-of-plane torsions
385	385		382	Ring deformation and OCC bending	18% ring (E) O-CC bending
	423		420	HNCC out-of plane torsion	43% ring (C) H-NCC out-of-plane torsion + 11% ring (D) H-NCC out-of-plane torsion
450	449	454	462	Ring deformation and HNCC out-of plane torsion	46% ring (E) CCC bending
	473		467	Ring twisting and hydrogen out-of-plane torsion	11% rings (C,D,E) CNC and CCC bending + 11% ring (C) H-NCC out-of-plane torsion
	490		489	Ring deformation out-of-plane	19% rings (B,C) CCCC torsions out-of-plane
497	498	500	502	Ring deformation	28% rings (A,B) CCC bending + 25% ring (B) C-N stretching

	507		518	Ring deformation out-of-plane	18% ring (B) O=CNC out-of-plane torsion
			528	Ring twisting	23% rings (C,D,E) CNC and CCC bending
	560		574	Ring deformation out-of-plane	40% ring (A) CCCC out-of-plane torsion
	568	571	581	Ring twisting	44% rings (B,C) O=CN bending
	587		609	Hydrogen out-of plane torsion	23% ring (E) O-CCC out-of-plane torsion + 20% ring (E) H-CCC out-of-plane torsion
			634	Ring deformation	49% ring (A) CCC bending
			643	Ring deformation	40% ring (B) CCN bending
			670	Ring deformation	39% ring (B) O=CN bending
680	680	680	689	Ring deformation out-of-plane	25% ring (C) NCCC out-of-plane torsion
			691	Ring deformation	50% ring (A) CCC bending
730	731	725	739	Ring deformation	17% ring (C) CNC bending + ring (A) CCC bending
	751		749	Ring deformation out-of-plane	29% rings (A,B) NCCC and CCCC out-of-plane torsions + 13% ring (E) CCCC out-of-plane torsion
	758		755	Ring deformation out-of-plane	44% rings (A,E) CCCC out-of-plane torsions
	776	771	770	Hydrogen out-of plane torsion	59% ring (A) H-CCC out-of-plane torsion
804	802	807	782	Ring deformation	43% ring (D) CNC bending + 20% ring (E) C=C stretching
	813		787	Ring deformation out-of-plane	61% rings (B,C) O=CNC out-of-plane torsions
	832		822	Ring deformation	20% ring (D) C-N stretching + 19% rings (D,E) CCC bending
			827	Hydrogen out-of plane torsion	67% ring (E) HCCC out-of plane torsion
			837	Hydrogen out-of plane torsion	70% rings (C,D) HCCC out-of-plane torsion
	851		850	Hydrogen out-of plane torsion	70% rings (C,D) HCCC out-of-plane torsion
872	871	873	888	Ring deformation	20% ring (B) CCC and CCN bending + 10% ring (A) CCC bending

	882	892	898	Ring deformation	32% rings (B,C) CCN bending
947	947	951	966	Ring deformation	24% rings (A,B) CCC and CCN bending
961	961		972	Ring deformation	35% ring (E) CCC bending + 10% ring (E) C-O stretching
	1027	1009	1011	Hydrogen out-of plane torsion	73% ring (A) HCCC out-of-plane torsion
	1040		1035	Ring deformation	31% ring (C) C-N stretching + 11% ring (C) HNC bending
	1061		1060	Ring deformation	56% ring (A) C=C stretching + 27% ring (A) HCC bending
	1098	1093	1116	Hydrogen bending	16% ring (D) HCN bending + 11% ring (E) HCC bending
			1146	Hydrogen bending	21% ring C-N (D) stretching + 17% rings (C,D) HNC bending + 12% ring (C) HCC bending
1132	1131	1124	1152	Hydrogen bending	27% ring (E) HCC bending + 11% ring (C) C-N stretching
1153	1153		1157	Hydrogen bending	40% rings (C,D,E) HCC bending
	1162		1177	Hydrogen bending	64% ring (A) HCC bending + 11% ring (A) C=C stretching
	1185		1200	Hydrogen bending	49% ring (E) H-OC bending + 11% ring (E) HCC bending
			1218	Hydrogen bending	27% ring (B) C-N stretching + 16% ring (B) HNC bending
1221	1221		1218	Ring deformation	17% ring (B) C=C stretching
			1242	Ring deformation and hydrogen bending	17% ring (D) C-N stretching + 14% ring (E) C-O stretching + 14% ring (E) HCC bending + 10% ring (D) HCC bending
1272	1271	1285	1268	Hydrogen bending	41% ring (E) HCC bending
			1270	Hydrogen bending	23% ring (A) HCC bending + 18% ring (B) HNC bending
			1298	Ring stretching	18% ring (C) C-C stretching + 11% (C) ring deformation + 10% ring (C) C-N stretching
	1302		1310	Ring stretching	36% ring (A) C=C stretching
			1322	Ring stretching	10% ring (E) C-O stretching
			1328	Hydrogen bending	15% ring (E) HCC bending + 15% ring (C) HNC bending

1354		1355	Hydrogen bending	12% ring (D) HCN bending	
1368	1370	1366	Hydrogen bending	34% ring (A) HCC bending + 12% ring (B) C-N stretching	
1379		1375	Hydrogen bending	21% ring (E) H-OC bending + 15% ring (D) C-N stretching	
		1390	Ring stretching	50% ring (E) C=C stretching	
1410		1419	Hydrogen bending	29% ring (B) HNC bending + 10% ring (A) HCC bending	
1463	1463	1463	1438	Ring stretching	19% ring (C) C-N stretching + 16% ring (C) HNC bending + 11% ring (D) C-N stretching
1482	1482		1480	Hydrogen bending and ring stretching	22% rings (C,D) HNC bending + 13% ring (D) C-N stretching
	1499		1509	Hydrogen bending	47% ring (A) HCC bending + 11% ring (A) CCC bending + 10% ring (B) C-N stretching
			1520	Hydrogen bending	21% ring (E) HCC bending + 15% ring (D) HCC bending
			1524	Ring twisting	35% ring (A) HCC bending + 32% ring (A) C=C stretching
1548	1549	1519	1550	Ring stretching	40% ring (E) C=C stretching
			1569	Ring stretching	51% ring (D) C=C stretching + 19% ring (D) HCN bending
	1608		1644	C=C stretching	49% C=C bridges between rings B-C and C-D stretching
			1652	Ring stretching	58% ring (A) C=C stretching
			1664	Ring stretching	44% ring (E) C=C stretching
			1691	Ring stretching	59% ring (A) C=C stretching
			1703	Ring stretching	53% ring (E) C=C stretching
			1711	Ring stretching	56% ring (C) C=C stretching
			1818	C=O stretching	70% ring (B) C=O stretching + 13% ring (C) C=O stretching
			1844	C=O stretching	72% ring (C) C=O stretching + 10% ring (B) C=O stretching

Section S3. SERS/SERRS detection of metabolites, bacterial culture on Au@agar and qPCR procedure.

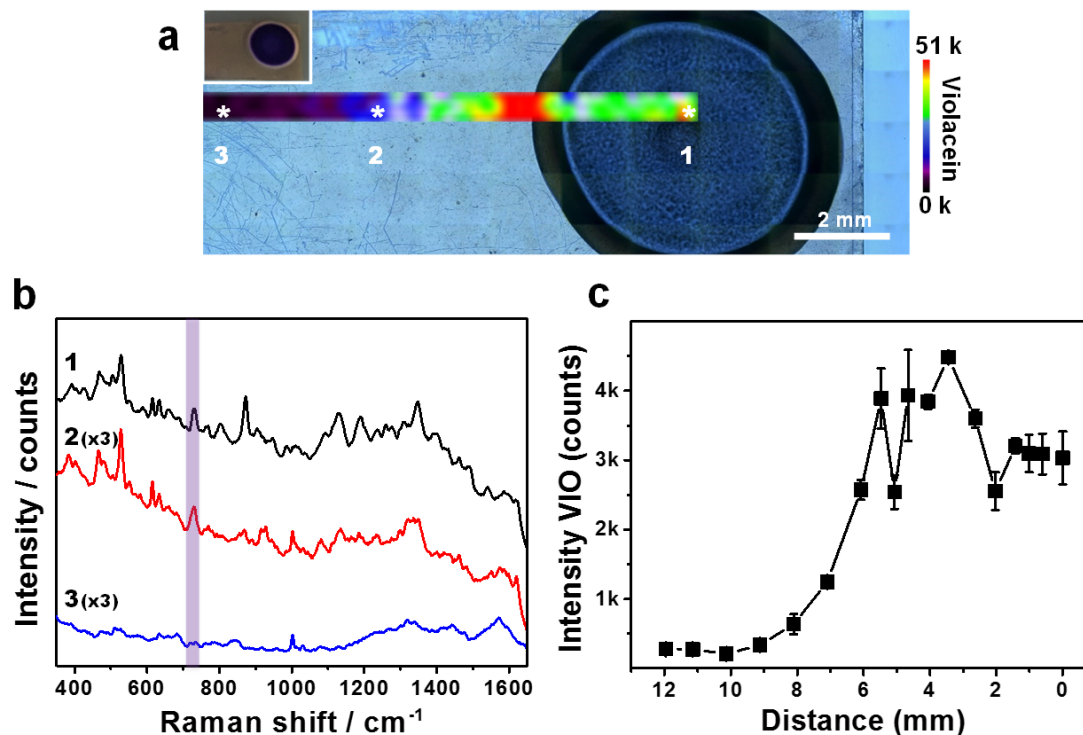


Figure S7. Analysis of violacein diffusion on Au@agar. (a) SERS map of violacein induced with 100 μM C4-AHL, recorded using the band at 727 cm^{-1} , indicated with a purple bar on the spectra shown in b. The inset shows a digital photograph of the bacterial colony. **(b)** SERS spectra measured in the points indicated with asterisks in a. **(c)** SERS intensities of violacein (727 cm^{-1}) measured in a as a function of distance from the center of the colony. The error bars show the standard deviation from three different measurements. The measurements were acquired with an excitation laser wavelength of 785 nm, 5x objective and laser power of 12.21 kW cm^{-2} , for 10 s.

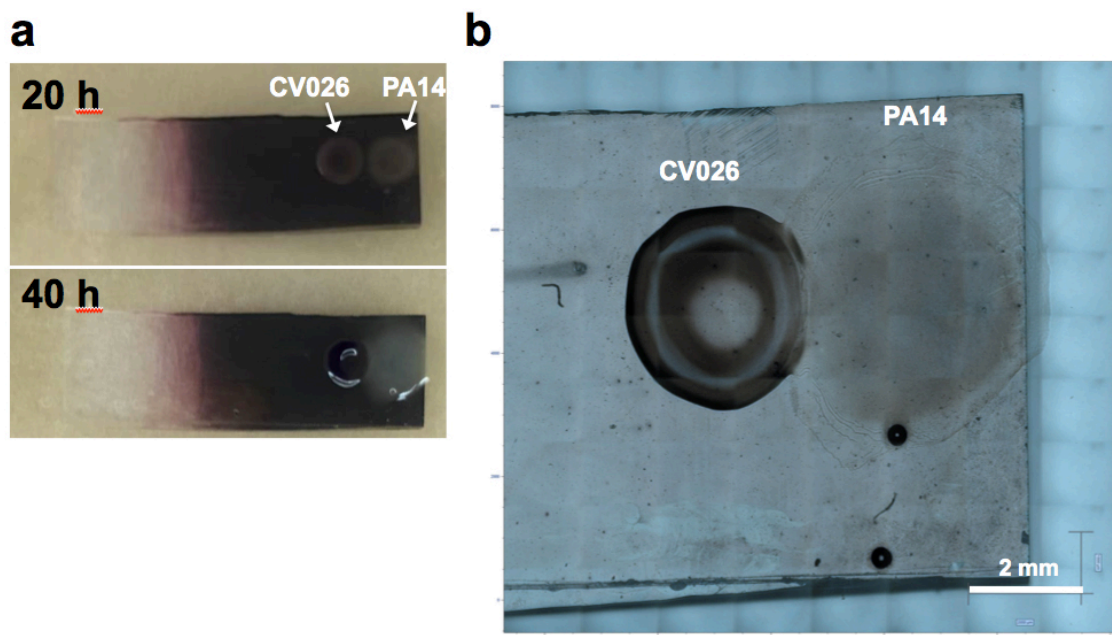


Figure S8. Co-culture of CV026 and PA14 on Au@agar. (a) Photographs of *C. violaceum* CV026 and *P. aeruginosa* PA14 colonies co-cultured on Au@agar taken at 20 and 40 hours. **(b)** Optical image acquired with the Raman microscope, for the 20 hour co-culture shown in a.

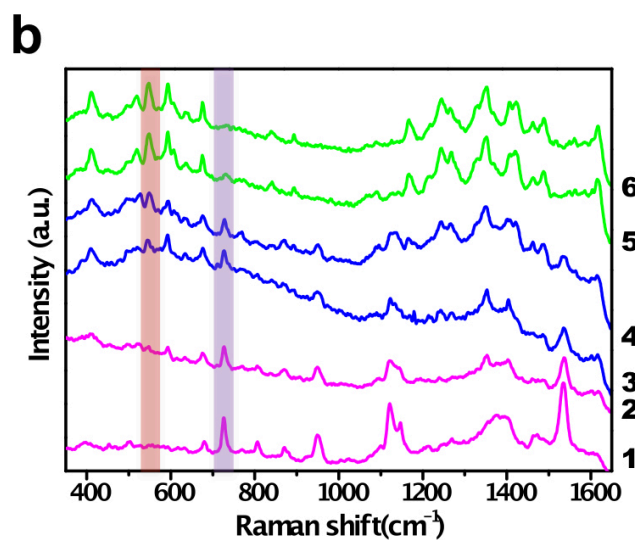
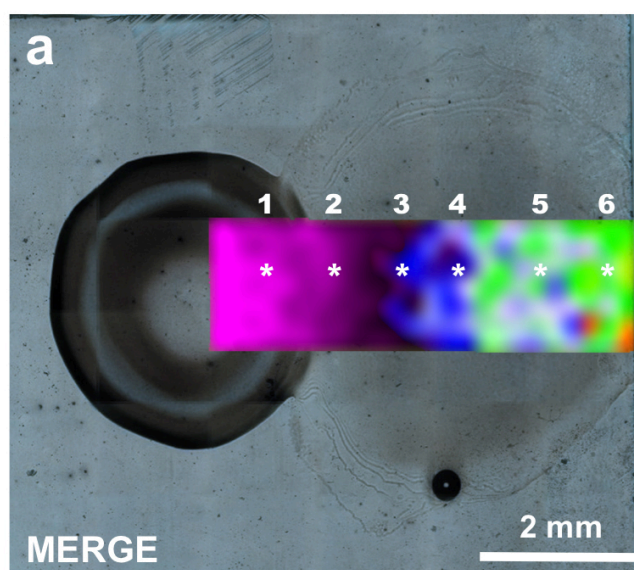


Figure S9. Detection of violacein and pyocyanin expressed in co-culture on Au@agar. (a) Overlay of SERS/SERRS mappings of violacein (727 cm^{-1}) and pyocyanin (544 cm^{-1}), respectively. **(b)** SERS/SERRS spectra recorded at the points indicated with asterisks in a.

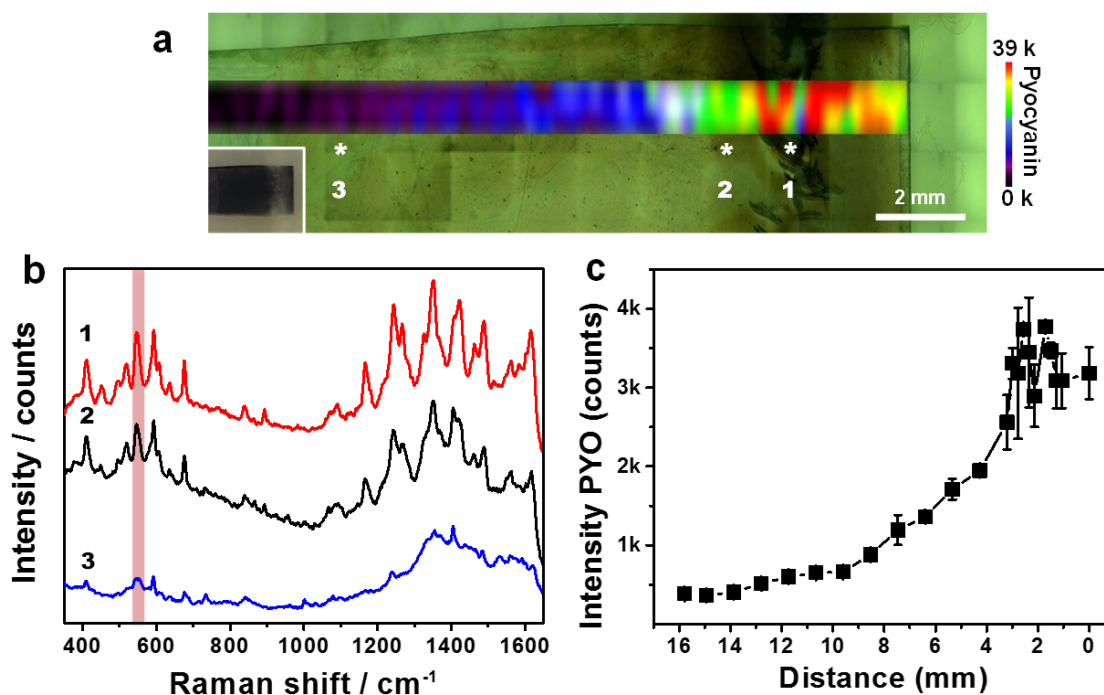


Figure S10. Analysis of pyocyanin diffusion on Au@agar. (a) SERRS mapping of pyocyanin produced by *P. aeruginosa* PA14 on Au@agar, recorded with the band at 544 cm^{-1} , indicated with a red bar on the spectra shown in B. The inset shows an optical photograph of the bacterial colony. (b) SERRS spectra measured at the points indicated with asterisks in A. (c) SERRS intensities of pyocyanin (544 cm^{-1}), measured in a as a function of distance from the center of the colony. The error bars show the standard deviation from three different measurements. The measurements were acquired with an excitation laser wavelength of 785 nm , $5\times$ objective and a laser power of 12.21 kW cm^{-2} for 10 s .

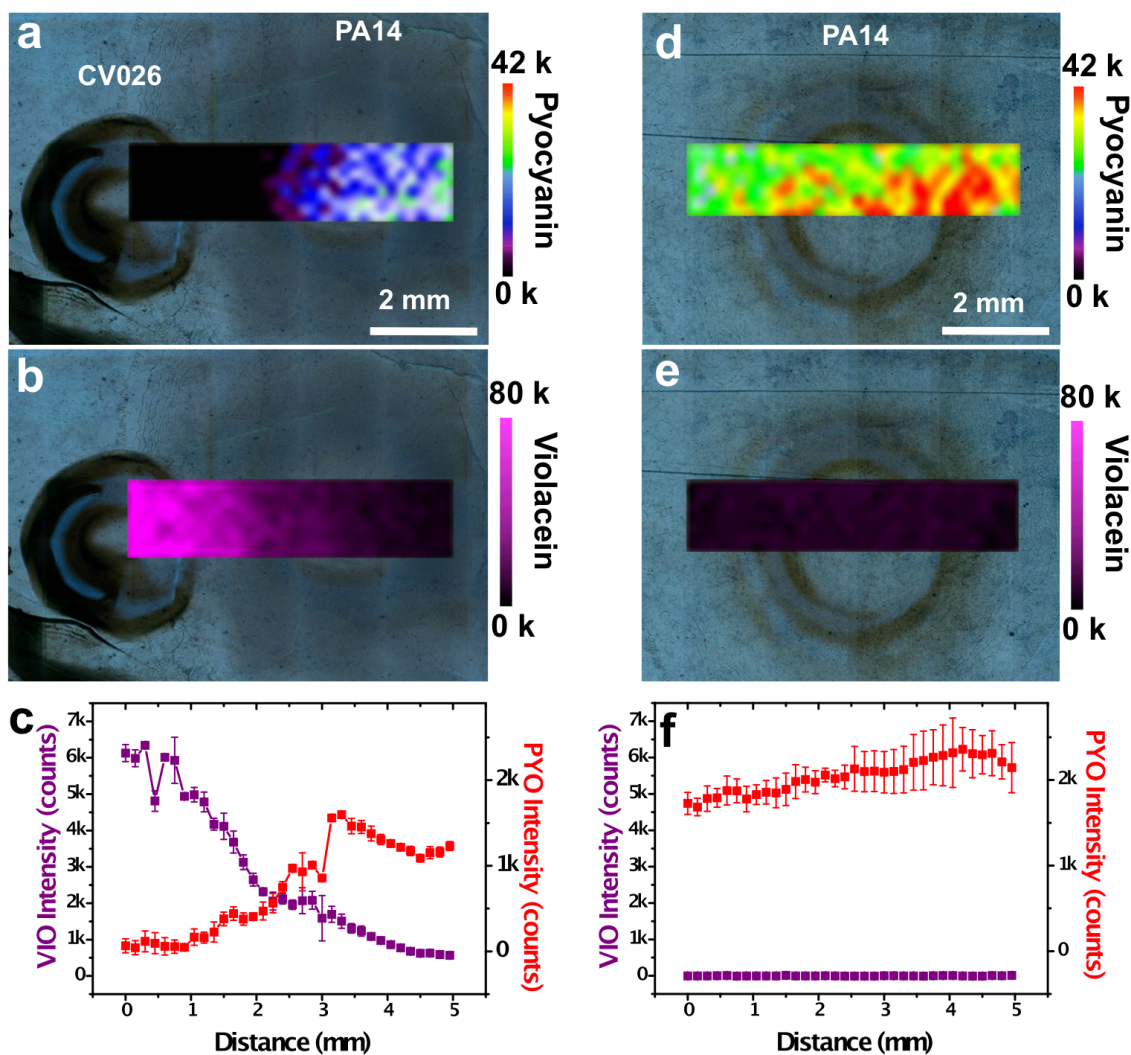


Figure S11. Quantification of SERS/SERRS relative intensities of bacterial metabolites in co-culture versus monoculture. (a) Optical image of the CV026 and PA14 co-culture, acquired with the Raman microscope, and photograph of the bacterial colonies (inset). (a,b) SERRS mapping of pyocyanin (544 cm^{-1}) (a) and SERS mapping of violacein (727 cm^{-1}) (b) in co-culture. (c) Average SERRS intensities of pyocyanin (red squares) and average SERS intensities of violacein (purple squares) measured from the mappings shown in a and b, respectively. Error bars show the standard deviation. (d,e) SERRS mapping of pyocyanin (544 cm^{-1}) (d) and SERS mapping of violacein (727 cm^{-1}) (e) in monoculture. (f) Average SERRS intensities of pyocyanin (red squares) and average SERS intensities of violacein (purple squares) measured from the mappings shown in d and e, respectively. Error bars show the standard deviation. All measurements were performed with an excitation laser wavelength of 785 nm, 5 \times objective and a laser power of 12.21 kW cm^{-2} for 10 s.

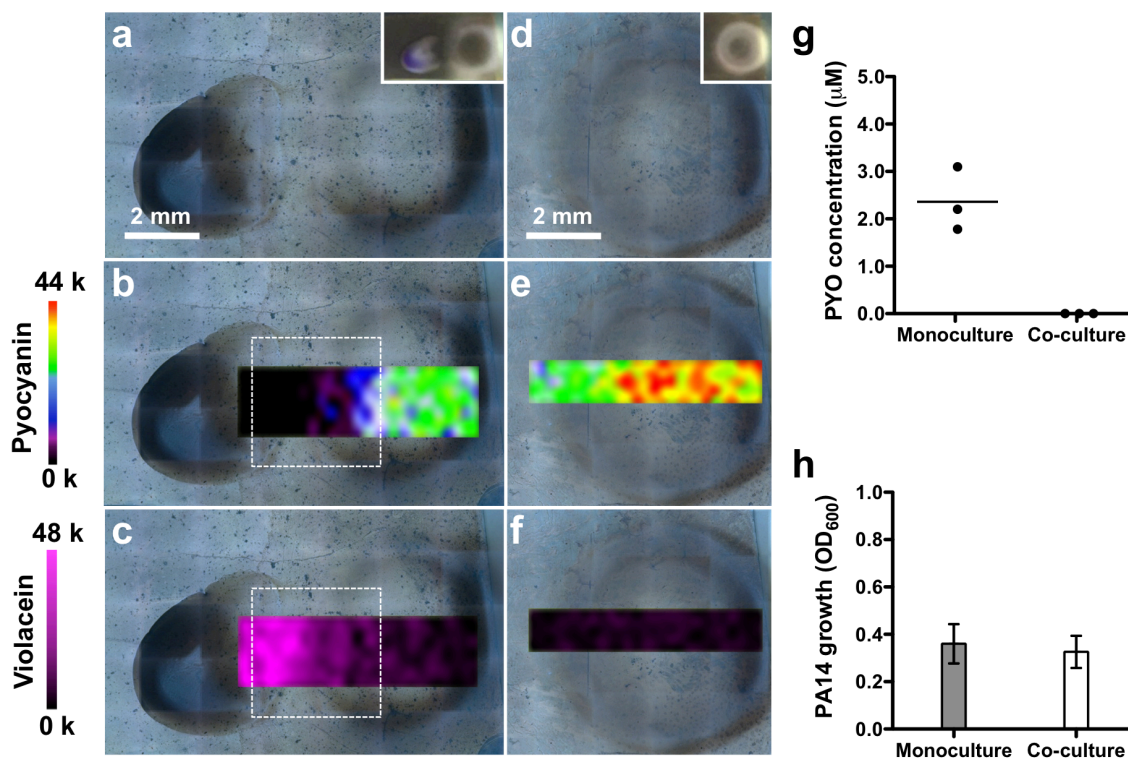


Figure S12. Imaging of pyocyanin and violacein expression, quantification of pyocyanin and determination of bacterial growth in co-culture versus monoculture. (a) Optical image of the CV026 and PA14 co-culture acquired with the Raman microscope, and photograph of the bacterial colonies (inset). (b, c) SERRS mapping of pyocyanin (544 cm^{-1}) (b) and SERS mapping of violacein (727 cm^{-1}) (c) in co-culture. The dashed rectangle indicates the confrontation zone (d) Optical image of the PA14 colony grown in monoculture acquired with the Raman microscope, and photograph of the colony (inset). (e, f) SERRS mapping of pyocyanin (544 cm^{-1}) (e) and SERS mapping of violacein (727 cm^{-1}) (f) in monoculture. All measurements were performed with an excitation laser wavelength of 785 nm, 5x objective and a laser power of 12.21 kW cm^{-2} for 10 s. (g) Quantification of pyocyanin (PYO) produced by PA14 colonies grown in monoculture or in co-culture by UV-Vis spectroscopy. Dark circles indicate the value obtained from biological triplicates ($n=6$, for each group). Straight line within the data points indicate average (h) Growth of PA14 cells in monoculture and in co-culture. Error bars indicate the standard deviation of biological triplicates.

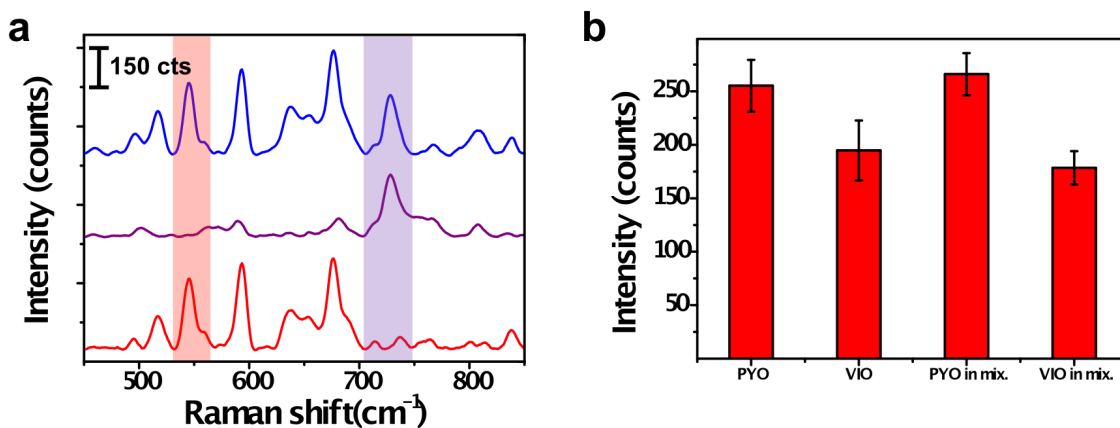


Figure S13. Analysis of the potential interaction of violacein and pyocyanin on Au@agar. Aqueous solutions (10 μL , 1 mM) of commercial pyocyanin or violacein in ethanol (100%) were combined, or diluted 1:1 in ethanol (100%) and allowed to diffuse on the substrate for 1 hour. **(a)** SERRS/SERS spectra of pyocyanin (red line), violacein (purple line) and their mixture (blue line). The red bars indicate pyocyanin-specific bands and the purple bar indicates a violacein-specific band. **(b)** Average intensities of 45 SERRS spectra of pyocyanin (544 cm^{-1}) or 45 SERS spectra of violacein (727 cm^{-1}) measured from the individual analytes or the mixture over a 0.05 mm^2 area. Spectra were measured with a $20\times$ objective, a maximum power of 0.03 kWcm^{-2} and an acquisition time of 10 s.

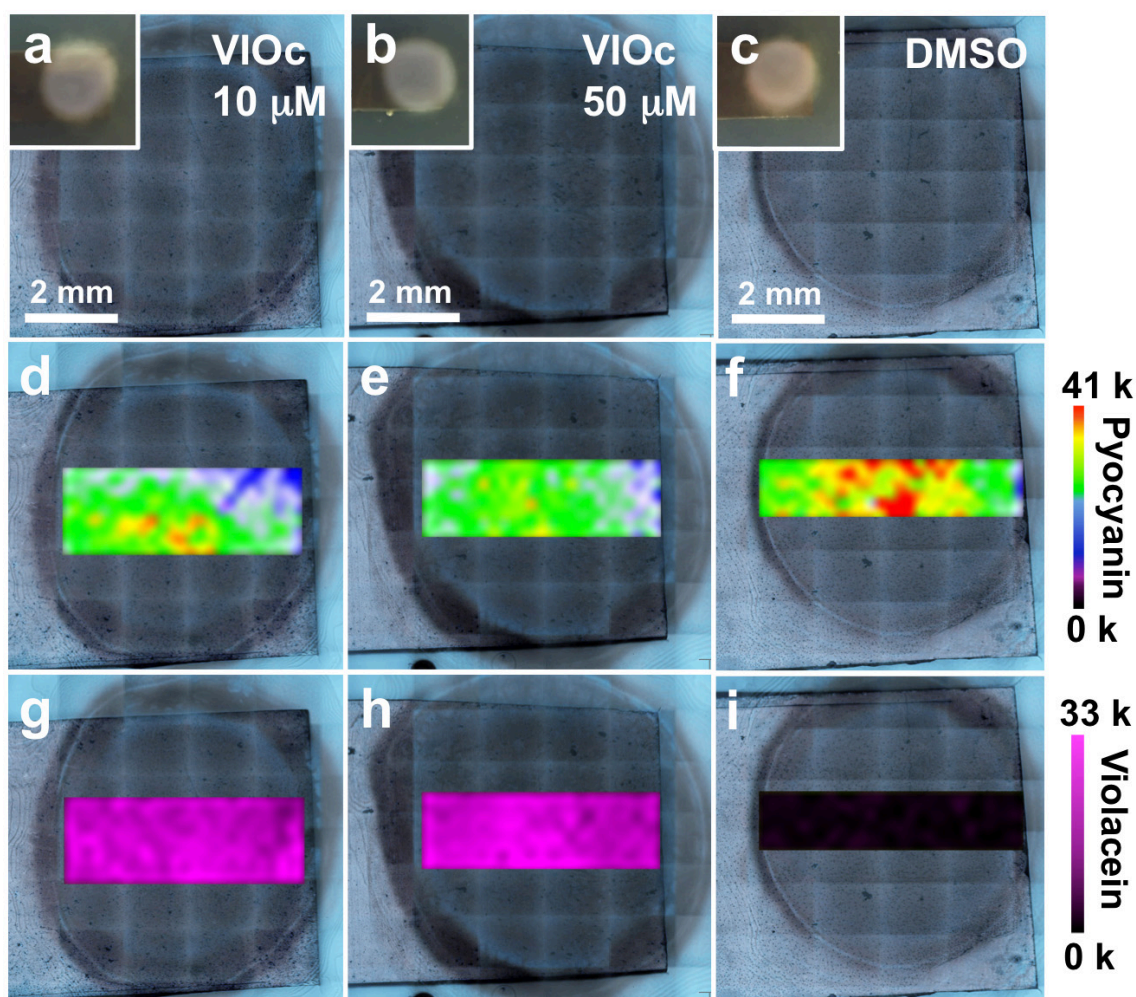


Figure S14. Imaging of pyocyanin expressed by *P. aeruginosa* colonies grown on commercial violacein (VIOc). (a, b and c) Optical images of PA14 colonies grown over VIOc (10 and 50 μM in DMSO 1%) or in DMSO (1%) acquired with the Raman microscope, and photographs of the bacterial colonies (insets). (d, e and f) SERRS mappings of pyocyanin (544 cm^{-1}) produced by PA14 bacteria grown over VIOc (10 μM and 50 μM in DMSO 1%) (d and e) or in DMSO (1%) (f). (g, h and i) SERS mappings of VIOc (727 cm^{-1}). All measurements were performed with an excitation laser wavelength of 785 nm, 5x objective and a laser power of 12.21 kW cm^{-2} for 10 s.

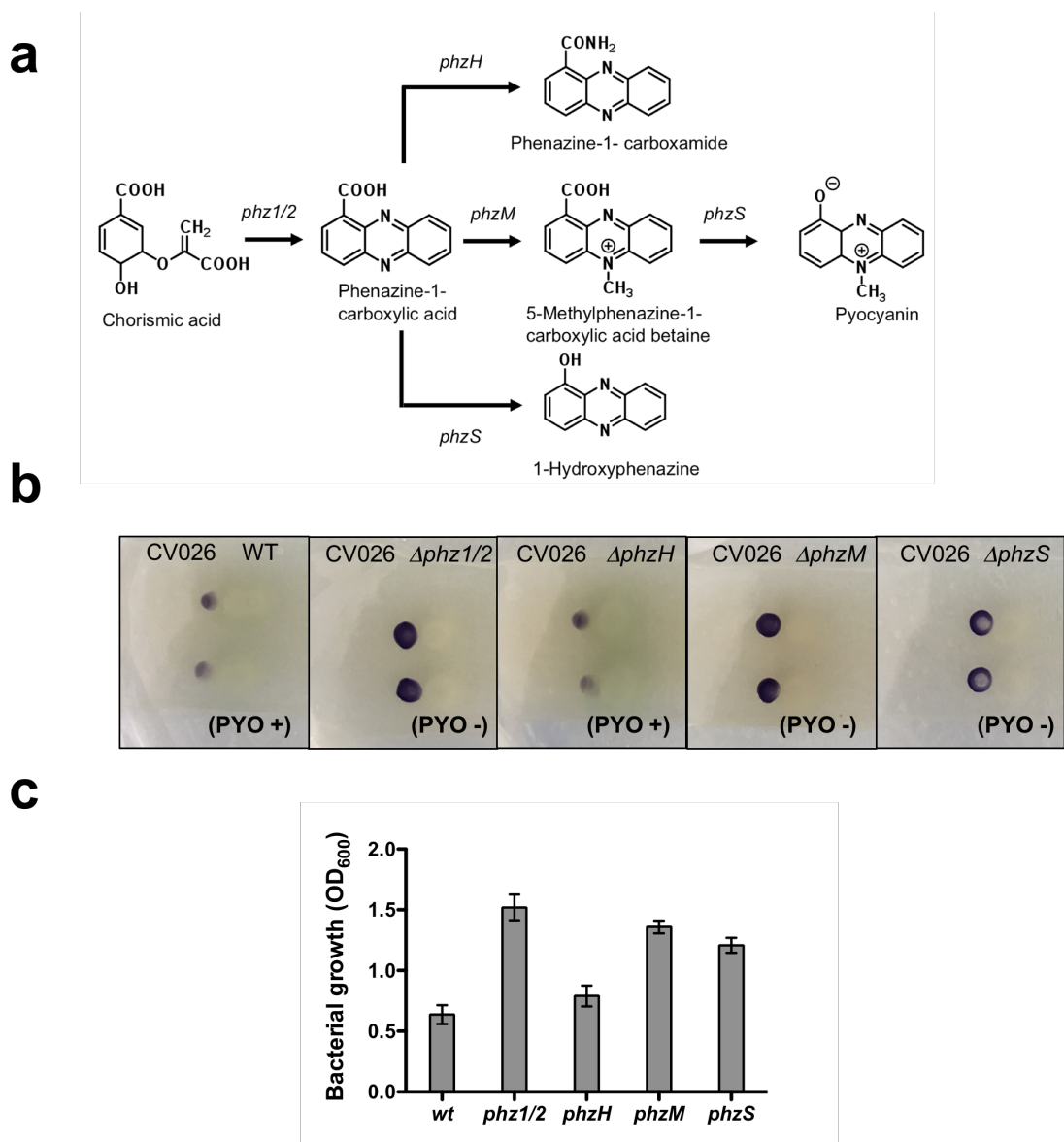


Figure S15. Analysis of phenazine influence on CV026 growth in co-culture. (a) Scheme of phenazine biosynthesis in *P. aeruginosa*. Chorismic acid is transformed into phenazine-1-carboxylic acid via two homologous *phz1* and *phz2* operons (*phz1/2*). This phenazine can be converted into phenazine-1-carboxamide, 5-methylphenazine-1-carboxylic acid betaine, 1-hydroxyphenazine and pyocyanin by the phenazine-modifying genes *phzH*, *phzM*, and *phzS*.³ **(b)** Photographs of co-cultures of CV026 with wild type (WT) or mutant *P. aeruginosa* PA14 strains deficient in genes involved in phenazine biosynthesis. **(c)** Growth analysis of CV026 colonies co-cultured with wild type (WT) and mutant *P. aeruginosa* PA14 strains as indicated.

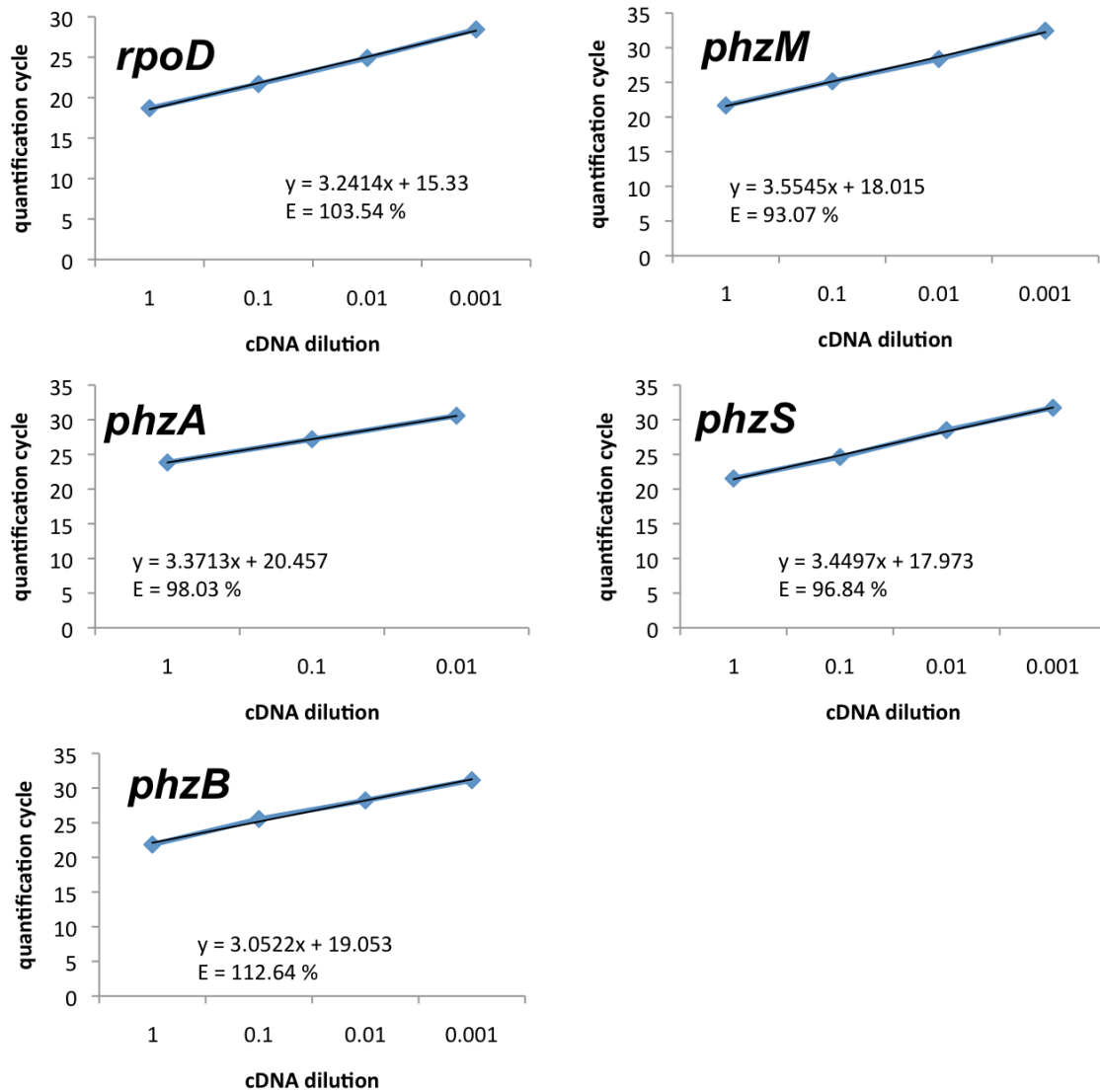


Figure S16. Calibration curves for primer pairs used in RT-qPCR experiments. Plots are labeled with gene names corresponding to the primer pair used. Linear regression equations and correlation coefficients were calculated using GraphPad Prism. E, primer efficiency.

Table S4. Bacterial strains

Bacterial strain	Relevant characteristics	Reference
<i>P. aeruginosa</i>		
PA14	Wild type. Clinical isolate UCBPP-PA14	4
PA14 $\Delta phz1/2$	Deletion of <i>phz1</i> and <i>phz2</i> operons	5
PA14 <i>phzH</i>	Transposon insertion mutant ID: 39981	6
PA14 <i>phzM</i>	Transposon insertion mutant ID: 40343	6
PA14 <i>phzS</i>	Transposon insertion mutant ID: 44099	6
<i>C. violaceum</i>		
CV026	Double mini-Tn5 mutant from <i>C. violaceum</i> ATCC 31532	7

Table S5. Sequence of primers

Gene	Locus ID ^a	Forward (5'-3')	Reverse (5'-3')	Amplicon length (bp)	Product T _m (°C) ^b
<i>phzA1</i> ^c	09480	TGCGAGAACCACTACATCCA	AACGGCTATTCCCAATGCAC	108	82
<i>phzB2</i> ^d	39960	GAACACCAAAGGCCAGGATC	TTGTCCTTGCCACGAATGAC	114	84
<i>phzM</i>	09490	GGTGGCCTTCGAGATCTTCC	GCCGTAGAACAGCACCATGT	115	89
<i>phzS</i>	09400	GGAAGACGTGTTGCCGTTCT	CGGGTACTGCAGGATCAACT	94	87
<i>rpoD</i>	07520	CAAGATCCGCAAGGTACTGA	GGTGGAGTCCTCGATGAAAT	106	83

^a Indicates NCBI Locus Tag of *P. aeruginosa* UNBPP-PA14.

^b Indicates product melting temperature (T_m) observed in the qPCR melt curve.

^c The primers do not discriminate between the two genes *phzA1* and *phzA2* of *phz1/2* operons in PA14.

^d The primers target specifically *phzB2* gene in PA14.

References

- (1) Gaussian 09, Revision A.02, Frisch, M. J.; Trucks, G. W.; Schlegel, H. B.; Scuseria, G. E.; Robb, M. A.; Cheeseman, J. R.; Scalmani, G.; Barone, V.; Mennucci, B.; Petersson, G. A.; Nakatsuji, H.; Caricato, M.; Li, X.; Hratchian, H. P.; Izmaylov, A. F.; Bloino, J.; Zheng, G.; Sonnenberg, J. L.; Hada, M.; Ehara, M. *et al.* Gaussian, Inc., Wallingford CT, 2009.
- (2) Jamroz, M. H. Vibrational Energy Distribution Analysis (Veda): Scopes and Limitations. *Spectrochim. Acta, Part A* **2013**, *114*, 220-230.
- (3) Jimenez, P. N.; Koch, G.; Thompson, J. A.; Xavier, K. B.; Cool, R. H.; Quax, W. J. The Multiple Signaling Systems Regulating Virulence in *Pseudomonas Aeruginosa*. *Microbiol. Mol. Biol. Rev.* **2012**, *76*, 46-65.
- (4) Rahme, L. G.; Stevens, E. J.; Wolfort, S. F.; Shao, J.; Tompkins, R. G.; Ausubel, F. M. Common Virulence Factors for Bacterial Pathogenicity in Plants and Animals. *Science* **1995**, *268*, 1899-1902.
- (5) Dietrich, L. E. P.; Price-Whelan, A.; Petersen, A.; Whiteley, M.; Newman, D. K. The Phenazine Pyocyanin Is a Terminal Signalling Factor in the Quorum Sensing Network of *Pseudomonas Aeruginosa*. *Mol. Microbiol.* **2006**, *61*, 1308-1321.
- (6) Liberati, N. T.; Urbach, J. M.; Miyata, S.; Lee, D. G.; Drenkard, E.; Wu, G.; Villanueva, J.; Wei, T.; Ausubel, F. M. An Ordered, Nonredundant Library of *Pseudomonas Aeruginosa* Strain Pa14 Transposon Insertion Mutants (Vol 103, Pg 2833, 2006). *Proc. Natl. Acad. Sci. U. S. A.* **2006**, *103*, 19931-19931.
- (7) McClean, K. H.; Winson, M. K.; Fish, L.; Taylor, A.; Chhabra, S. R.; Camara, M.; Daykin, M.; Lamb, J. H.; Swift, S.; Bycroft, B. W.; Stewart, G. S. A. B.; Williams, P. Quorum Sensing and Chromobacterium *Violaceum*: Exploitation of Violacein Production and Inhibition for the Detection of N-Acylhomoserine Lactones. *Microbiol.* **1997**, *143*, 3703-3711.